LETTER

Radiative heat transfer in the extreme near field

Kyeongtae Kim[1]†*, Bai Song[1]*, Víctor Fernández-Hurtado[2]*, Woochul Lee[1], Wonho Jeong[1], Longji Cui[1], Dakotah Thompson[1], Johannes Feist[2], M. T. Homer Reid[3], Francisco J. García-Vidal[2,4], Juan Carlos Cuevas[2], Edgar Meyhofer[1] & Pramod Reddy[1,5]

Radiative transfer of energy at the nanometre length scale is of great importance to a variety of technologies including heat-assisted magnetic recording[1], near-field thermophotovoltaics[2] and lithography[3]. Although experimental advances have enabled elucidation of near-field radiative heat transfer in gaps as small as 20–30 nanometres (refs 4–6), quantitative analysis in the extreme near field (less than 10 nanometres) has been greatly limited by experimental challenges. Moreover, the results of pioneering measurements[7,8] differed from theoretical predictions by orders of magnitude. Here we use custom-fabricated scanning probes with embedded thermocouples[9,10], in conjunction with new microdevices capable of periodic temperature modulation, to measure radiative heat transfer down to gaps as small as two nanometres. For our experiments we deposited suitably chosen metal or dielectric layers on the scanning probes and microdevices, enabling direct study of extreme near-field radiation between silica–silica, silicon nitride–silicon nitride and gold–gold surfaces to reveal marked, gap-size-dependent enhancements of radiative heat transfer. Furthermore, our state-of-the-art calculations of radiative heat transfer, performed within the theoretical framework of fluctuational electrodynamics, are in excellent agreement with our experimental results, providing unambiguous evidence that confirms the validity of this theory[11–13] for modelling radiative heat transfer in gaps as small as a few nanometres. This work lays the foundations required for the rational design of novel technologies that leverage nanoscale radiative heat transfer.

Radiative heat transfer in the far field[14], that is, at gap sizes larger than Wien's wavelength ($\sim$10 μm at room temperature), is well established. However, near-field radiative heat transfer (NFRHT), where the gap sizes are smaller than Wien's wavelength, remains relatively unexplored[15]. Over the past decade, a series of technical advances have enabled experiments[4–6] for gap sizes as small as 20 nm to study NFRHT and broadly verify the validity of a theoretical framework called fluctuational electrodynamics[11,16–18] for modelling NFRHT. In contrast, recent experiments[7,8] of extreme (e)NFRHT with single-digit nanometre gap sizes ($<$10 nm) between gold (Au) surfaces have questioned the validity of fluctuational electrodynamics and have raised the question of whether additional mechanisms, even of non-radiative origin such as phonon tunnelling[19], could dominate the heat transfer in this regime. In addition, some newer computational eNFRHT studies[20] on dielectrics have suggested that the local form of fluctuational electrodynamics, in which one assumes the dielectric properties of the media to be local in space, is inadequate for modelling eNFRHT. Yet other computations[21] on dielectrics have asserted that such non-local effects are irrelevant even for gap sizes as small as 1 nm. This disagreement is of great concern because understanding eNFRHT is critical for the development of a range of novel technologies[1–3]. Here, we present experimental and computational results that both demonstrate marked increases in heat fluxes in the extreme near field and establish the validity of fluctuational electrodynamics for modelling/predicting eNFRHT for dielectric as well as metal surfaces in gap sizes as small as a few nanometres.

Experimental elucidation of radiative heat transfer across few-nanometre-sized gaps is exceedingly difficult, owing to numerous technical challenges in creating and stably maintaining such gaps while simultaneously measuring minute (pW) heat currents across them. One key innovation used in this work to overcome the technical challenges was to leverage highly sensitive, custom-fabricated probes with embedded Au–Cr thermocouples (Fig. 1a–c), called scanning thermal microscopy (SThM) probes[9]. The SThM probes were fabricated by deposition of multiple metal and dielectric layers to create a nanoscopically small Au–Cr thermocouple at the very end of the tip. Our probes were optimized to have both a high thermal resistance[22] ($R_P \approx 10^6$ K W^{-1}) and stiffness[9] ($>$4 N m^{-1}), and were coated with a desired dielectric (silica (SiO$_2$) or silicon nitride (SiN)) or metal (Au) layer. The resulting probes have tip diameters ranging from 350 nm to 900 nm (for details see Fig. 1b and Supplementary Figs 1–3).

The basic strategy for quantifying NFRHT is to record the tip temperature, via the embedded nanoscale thermocouple, which rises in proportion to the radiative heat flow when the tip is displaced towards a heated substrate. To eliminate conductive and convective heat transfer and to remove any water adsorbed to the surfaces, all measurements were performed in an ultra-high vacuum (UHV) using a modified scanning probe microscope (RHK UHV 7500) housed in an ultra-low-noise facility (see Supplementary Information). In performing the measurements, the substrate is heated to an elevated temperature ($T_S = 425$ K) while the SThM probe, mounted in the scanner of the scanning probe microscope, is connected to a thermal reservoir maintained at a temperature $T_R = 310$ K. The spatial separation between the probe and the substrate is reduced at a constant rate of 0.5 nm s^{-1} from a gap size of 50 nm until probe–substrate contact. During this process the temperature difference between the tip (T_P) and the reservoir (T_R), $\Delta T_P = T_P - T_R$, is monitored (see Supplementary Information) via the embedded thermocouple, while the deflection of the cantilever is concurrently measured optically via an incident laser (Fig. 1a).

A typical deflection trace for a SiO$_2$-coated tip approaching a SiO$_2$-coated surface is shown in Fig. 2a. From the deflection trace it is apparent that the gap size can be controllably reduced to values as small as $\sim$2 nm, below which the tip rapidly 'snaps' towards the substrate and makes contact (see Supplementary Information). This instability is created by attractive forces between the tip and the substrate that arise owing to Casimir and/or electrostatic forces. Figure 2a shows the simultaneously measured ΔT_P, which represents the sudden increase in temperature that occurs when the tip snaps into the substrate. This rapid increase in tip temperature ($\sim$2 K) upon mechanical contact is due to heat conduction, via the solid–solid contact, from the hot substrate (425 K) to the tip of the SThM probe, the temperature of

[1]Department of Mechanical Engineering, University of Michigan, Ann Arbor, Michigan 48109, USA. [2]Departamento de Física Teórica de la Materia Condensada and Condensed Matter Physics Center (IFIMAC), Universidad Autónoma de Madrid, Madrid 28049, Spain. [3]Department of Mathematics, Massachusetts Institute of Technology, Cambridge, Massachusetts 02139, USA. [4]Donostia International Physics Center (DIPC), Donostia/San Sebastián 20018, Spain. [5]Department of Materials Science and Engineering, University of Michigan, Ann Arbor, Michigan 48109, USA. †Present address: Department of Mechanical Engineering and Robotics, Incheon National University, Incheon 22012, South Korea. *These authors contributed equally to this work.
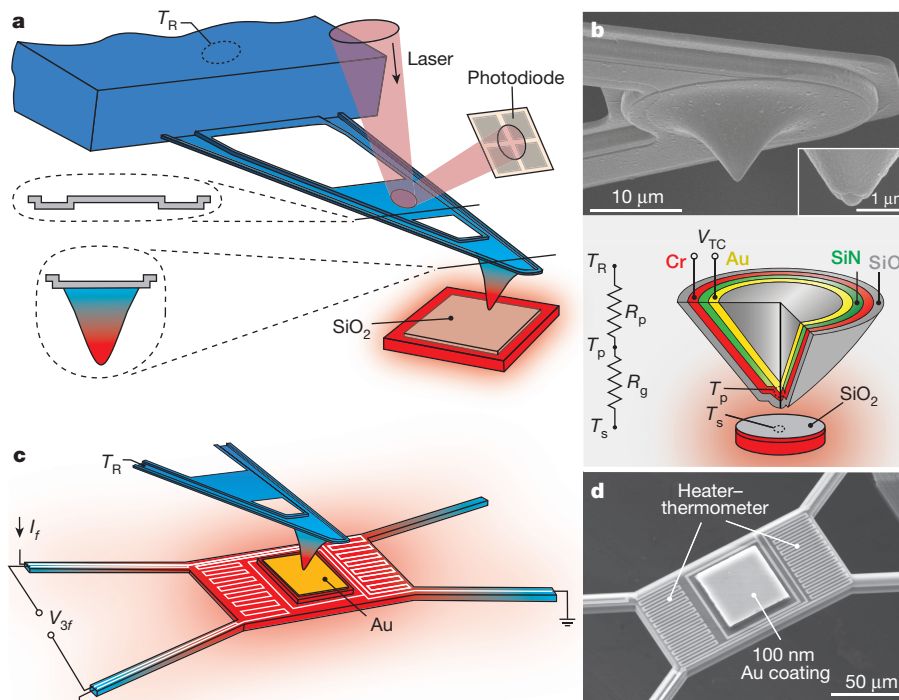
Figure 1 | Experimental set-up and SEM images of SThM probes and suspended microdevices. a, Schematic of the experimental set-up, in which an SThM probe is in close proximity to a heated substrate (insets show cross-sections of the SThM probe). The scenario for SiO_2 measurements is shown (the coating on the substrate is replaced with SiN and Au in other experiments). **b**, SEM image (top) of a SThM probe. The inset shows an SEM image of the hemispherical probe tip, which features an embedded Au–Cr thermocouple from which the thermoelectric voltage V_{TC} is measured. The bottom panel illustrates a schematic cross-section for a SiO_2-coated probe used in SiO_2 measurements. For SiN and Au measurements, the outer SiO_2 coating is appropriately substituted as explained in Supplementary Information. A resistance network that describes the thermal resistance of the probe (R_P) and the vacuum gap ($R_g = (G_{eNFRHT})^{-1}$), as well as the temperatures of the substrate (T_S), tip (T_P) and reservoir (T_R) is also shown. **c**, Schematic showing the measurement scheme used for high-resolution eNFRHT measurements of Au–Au. The amplitude of the supplied sinusoidal electric current is I_f, the sinusoidal temperature oscillations at $2f$ are related to the voltage output V_{3f}. **d**, SEM image of the suspended microdevice featuring the central region coated with Au and a serpentine Pt heater–thermometer.

which is $\sim$400 K (heating by the incident laser results in an elevated temperature).

The tight temporal correlation between the mechanical snap-in and the temperature jump of the probe makes it possible to identify tip–substrate contact solely on the basis of temperature signals. In Fig. 2b, the recorded tip temperature is shown as a probe approaches a heated substrate with the laser beam turned off. The recorded temperature signals with and without laser tracking are basically identical (Fig. 2a, b), except that the magnitude of the jump reflects the tip–substrate temperature difference with and without laser excitation. Thus, mechanical contact can be readily detected from the robust temperature jump without laser excitation, thereby avoiding probe heating and laser interference effects. Therefore, we performed all experiments by first estimating the snap-in distance using the optical scheme and subsequently turning the laser off to perform eNFRHT measurements (see Supplementary Information for the measurement of gap size and snap-in distance).

To determine the gap (d)-dependent near-field radiative conductance (G_{eNFRHT}), we measured ΔT_P and directly estimated G_{eNFRHT} from $G_{eNFRHT}(d) = \Delta T_P/[R_P(T_S - T_R - \Delta T_P)]$, where R_P is the thermal resistance of the probe, which was experimentally determined as described in Supplementary Information (Supplementary Fig. 7) to be 1.6×10^6 K W^{-1} and 1.3×10^6 K W^{-1} for the SiO_2- and SiN-coated probes, respectively. The measured conductance of the gaps for SiO_2 and SiN surfaces is shown in Fig. 3a and b, respectively. It can be seen that G_{eNFRHT} increases monotonically until the probe snaps into contact (gap size at snap-in is $\sim$2 nm for both SiO_2 and SiN measurements; see Supplementary Information and Supplementary Fig. 6). Furthermore, it can be seen that the eNFRHT is larger for experiments performed with SiO_2. These measurements represent

the first observation of eNFRHT in single-digit nanometre-sized gaps between dielectric surfaces. We compared these results to our computational predictions based on fluctuational electrodynamics, assuming local-dielectric properties (see details later), and found very good agreement (blue lines in Fig. 3a, b).

The remarkable agreement between eNFRHT measurements and computational predictions raises important questions with regards to recent experiments[7] investigating eNFRHT between Au surfaces, which suggested strong disagreements ($\sim$500-fold) between predictions of fluctuational electrodynamics and the results of experiments. One may wonder if the good agreement reported above is unique to eNFRHT between polar dielectric materials. To answer this question unambiguously, we performed additional eNFRHT measurements with Au-coated probes and substrates. The measured conductance in these experiments is shown in Fig. 3c. It can be seen that the measured G_{eNFRHT} with decreasing gap size remains comparable to the noise floor of $\sim$220 pW K^{-1} for Au-coated probes at an applied temperature differential of $\sim$115 K (see Supplementary Information) and is much smaller than that observed for polar dielectrics. These measurements set an upper bound of $\sim$250 pW K^{-1} for G_{eNFRHT} in our Au–Au experiments. This result is particularly surprising because previous studies that used probes with smaller diameters and lower thermal resistances[7,23] ($(23–54) \times 10^3$ K W^{-1} and $\sim$10^6 K W^{-1}, implying a lower sensitivity than our probes) reported conductances $>$40 nW K^{-1}, which are at least two orders of magnitude larger than conductances measured by us and predicted by theory.

To resolve this contradiction we needed to improve the resolution of our conductance measurements by more than an order of magnitude (see Supplementary Information and Supplementary
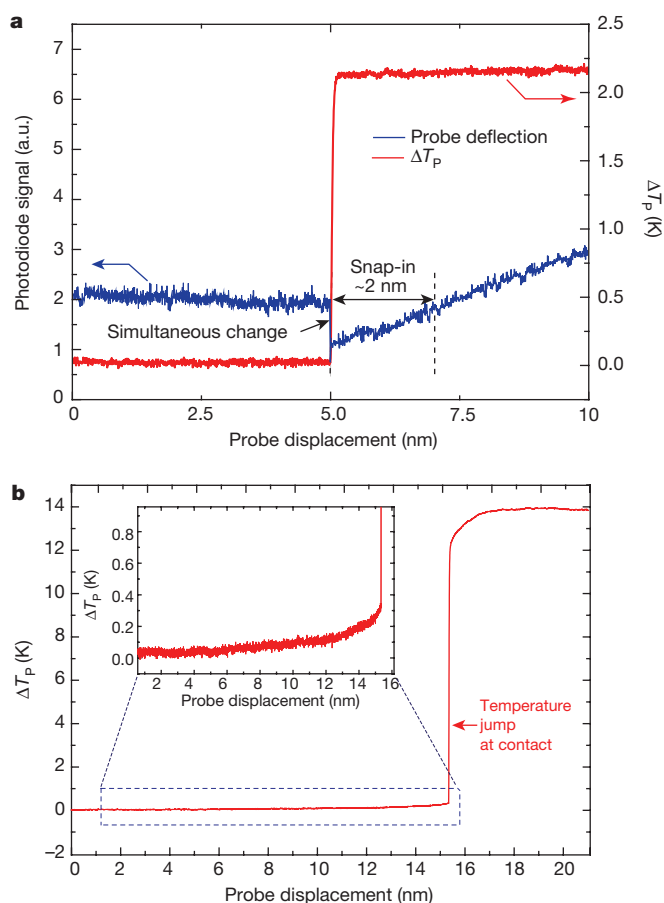
Figure 2 | Detection of mechanical contact from deflection and temperature signals. a, Data from an experiment in which a SiO_2-coated probe at about 400 K (heated by the incident laser) is displaced towards a heated SiO_2 substrate at 425 K. The deflection of the scanning probe (blue), reported in arbitrary units (a.u.), and rise in temperature of probe, ΔT_P (red), are shown. The sudden decrease in the deflection signal due to snap-in coincides with a simultaneous increase in the tip temperature due to conduction of heat from the hot substrate to the cold tip, clearly showing that contact can be readily detected by the large temperature jump. The snap-in distance is seen to be ~2 nm. **b**, Measured ΔT_P when an unheated probe (310 K, laser turned off) is displaced towards the substrate. A sudden increase in the tip temperature is seen when the cold tip contacts the substrate. Inset shows the increase in the tip temperature due to eNFRHT.

Fig. 8 for details). This was accomplished by using a new microdevice (see Fig. 1c, d and Supplementary Figs 4, 5, 9, 10 for details of device fabrication and characterization) that features a suspended island whose temperature can be readily modulated at $f = 18$ Hz (see Supplementary Information). Sinusoidal electric currents (9 Hz) supplied to the embedded electrical heater resulted in sinusoidal temperature oscillations at the second harmonic with amplitude ($\Delta T_{S,f = 18 Hz}$) that was accurately measured using a lock-in technique[6,24] (see Supplementary Information). To characterize eNFRHT, we positioned a Au-coated SThM probe (30 nm Au thickness) in close proximity to the surface of the microfabricated device, which features a suspended region that is $50 \mu m \times 50 \mu m$ large and was coated with 100 nm of Au. The amplitude of temperature modulation of the probe ($\Delta T_{P,f = 18 Hz}$), due to eNFRHT, was measured at various gap sizes (see Supplementary Information) in a bandwidth of 0.78 mHz. Given the low noise in this bandwidth it was possible to resolve temperature changes as small as ~20 μK, which corresponds to a conductance noise floor of ~6 pW K^{-1}, when $\Delta T_{S,f = 18 Hz}$ is 5 K (see Supplementary Information section 7 for details of the noise characterization). The measured $\Delta T_{P,f = 18 Hz}$ values were

used to estimate G_{eNFRHT} (Fig. 3d) via: $G_{eNFRHT}(d) = \Delta T_{P,f = 18 Hz}/[R_{P,Au}(\Delta T_{S,f = 18 Hz} - \Delta T_{Pf = 18 Hz})]$, where $R_{P,Au} = 0.7 \times 10^6$ K W^{-1} is the thermal resistance of the Au-coated probe (see Supplementary Information and Supplementary Fig. 7). The smallest gap size at which measurements could be accomplished is ~3 nm and is limited by both snap-in and deflections of the microdevice due to periodic thermal expansion resulting from bimaterial effects (see Supplementary Fig. 11). The measured G_{eNFRHT} (Fig. 3d) is indeed much smaller than that obtained with SiO_2 (Fig. 3a) and SiN (Fig. 3b) films. In contrast to previous experiments[7], our measured G_{eNFRHT} for Au–Au surfaces is in excellent agreement with the predictions of fluctuational electrodynamics (solid line in Fig. 3d).

To obtain insight into our experimental results, we used a fluctuating-surface-current formulation of the radiative heat transfer problem[13,25] combined with the boundary element method, as implemented by us in the SCUFF-EM solver[26]. This allows NFRHT calculations between bodies of arbitrary shape and provides numerically exact results within the framework of fluctuational electrodynamics in the local approximation[13,25]. For our calculations, we characterized the dielectric function for SiN, whereas the dielectric functions for SiO_2 and Au were taken from previous work (see Supplementary Information section 12 and Supplementary Fig. 12). To simulate our experiments accurately, we considered the tip–substrate geometries shown in the left insets of Fig. 4c, d. Here, the tip has a conical shape and ends in a spherical cap whose radius was obtained from scanning electron microscope (SEM) images of the probes (see Supplementary Figs 1–3). In our simulations, we included sufficiently large areas of the probe's conical part and the substrate such that the results do not depend on their finite size (see Supplementary Information section 14 and Supplementary Fig. 13). To maintain high fidelity to the experimental conditions, we also accounted for the small roughness of our probes by including random Gaussian-correlated noise in the tip profile (Fig. 4c, d). More precisely, the maximum protrusion height on the tip and the correlation length between protrusions were chosen to be 10 nm and 17 nm, respectively, on the basis of the surface characteristics observed in the SEM images (Supplementary Figs 1–3). We investigated the effect of surface roughness by computing G_{eNFRHT} for every material from 15 different tip–substrate ensembles with roughness profiles generated as described earlier. The computational results for the different materials are presented in Fig. 3a, b, d. As pointed out earlier, we indeed find very good agreement between computation and experiment without any adjustable parameters.

To elucidate the underlying physical mechanism and explain the differences in eNFRHT between different material combinations, we computed the spectral conductance (heat conductance per unit of energy) for several gap sizes as shown in Fig. 4a, b for SiO_2 and Au, respectively (see Supplementary Fig. 14 for SiN results). In Fig. 4a, one can see that the dominant contributions to the spectral conductance of SiO_2 come from two narrow energy ranges centred around ~0.06 eV and ~0.14 eV, which correspond to the energies of the transverse optical phonons of SiO_2. This strongly suggests that for SiO_2, eNFRHT is dominated by surface phonon polaritons (SPhPs), as previously found for larger gaps[6,27,28]. In turn, this explains the marked decrease in heat transfer as the gap size increases, which is a consequence of the rapid decrease in the number of available surface electromagnetic modes for radiation to tunnel across the vacuum gap. In contrast, eNFRHT for Au exhibits a rather broad spectral conductance that decays more slowly with gap size (Fig. 4b). This slow decay is reminiscent of the situation encountered in a plate–plate geometry[29] where NFRHT is dominated by frustrated internal reflection modes, that is, by modes that are evanescent in the vacuum gap but are propagating inside the Au tip and substrate whose contribution saturates for gaps below the skin depth[29], which for Au is around 25 nm. This naturally explains the weaker dependence of eNFRHT on gap size observed in our Au–Au measurements. The fundamental difference in eNFRHT between dielectrics and metals is also apparent from the computed Poynting-flux
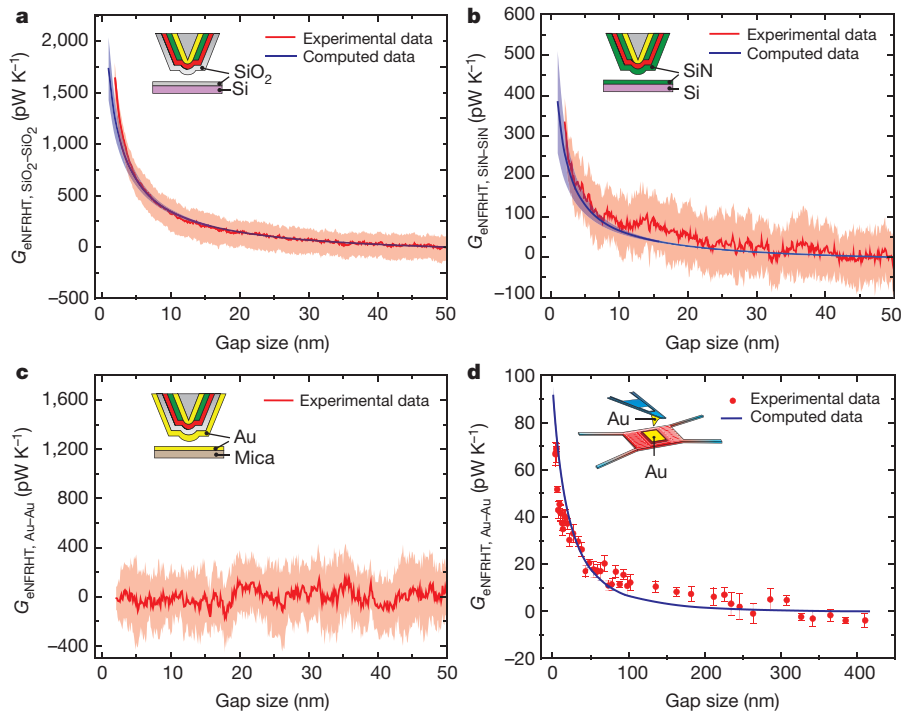
Figure 3 | Measured extreme near-field thermal conductances for dielectric and metal surfaces. a, Measured near-field radiative conductance between a SiO$_2$-coated probe (310 K) and a SiO$_2$ substrate at 425 K. The red solid line shows the average conductance from 15 independent measurements, the light red band represents the standard deviation. The blue solid line shows the average of the computed radiative conductance for 15 different tips with stochastically chosen roughness profiles (root-mean-squared roughness of ~10 nm) and a tip diameter (450 nm) obtained from SEM images of the probe.

The blue shaded region represents the standard deviation in the calculated data. **b**, **c**, Same as **a**, but for SiN–SiN and Au–Au, respectively. The tip diameter is 350 nm for the SiN-coated tip. Computed results are not included for Au–Au. **d**, Near-field conductance from experiments with a Au-coated probe and a suspended microdevice. Red dots represent the average from 10 different measurements (temperature periodically modulated at 18 Hz); the error bars represent the standard deviation. The blue solid line represents the computed conductance (tip diameter is 900 nm).
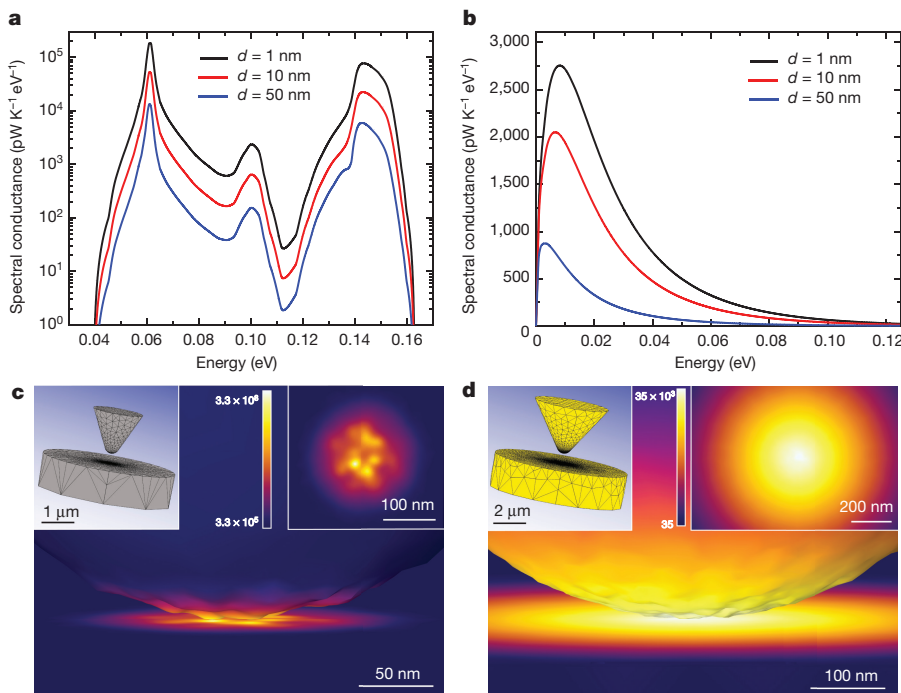

Figure 4 | Spectral conductance and spatial distribution of the Poynting flux. a, Spectral conductance as a function of energy for a SiO$_2$ tip–substrate geometry for three different gap sizes. The tip diameter is 450 nm, and the reservoir temperatures are 310 K for the tip and 425 K for the substrate. Notice the logarithmic scale in the vertical axis. **b**, Same as **a**, but for Au. In this case, the tip radius is 450 nm, and the tip and substrate temperatures are 300 K and 301 K, respectively. **c**, Surface-contour plot showing the spatial distribution of the Poynting-flux pattern on the

surface of the bodies for the SiO$_2$ tip–substrate geometry corresponding to that in **a** with a gap of 1 nm. The colour scale is in units of W (K eV m^2)$^{-1}$ and the plot was computed at an energy of 61 meV, which corresponds to the maximum of the spectral conductance. The right inset shows the corresponding surface heat flux on the substrate; the left inset displays the whole tip–substrate geometry simulated, including the mesh used in the calculations. **d**, Same as **c**, but for Au. In this case the surface-contour plot was computed at 9 meV, the maximum of the spectral conductance.

patterns on the surfaces (Fig. 4c, d), which show that eNFRHT in the SiO_2 case is much more concentrated in the tip apex than it is in the Au case. This difference reflects the fact that in a polar dielectric, such as SiO_2, eNFRHT has a very strong distance dependence due to the excitation of SPhPs with a penetration depth comparable to the gap size[6]. Given these differences between metals and dielectrics, it is not surprising that Au–Au eNFRHT is relatively insensitive to small surface roughness (see Supplementary Fig. 15). For this reason, the large differences between our results for Au and those of previous work[7,8], which disagree with the predictions of fluctuational electrodynamics, cannot be attributed to differences in the surface roughness. Our computational results, when compared with our experimental data, provide unambiguous evidence that fluctuational electrodynamics accurately describes eNFRHT.

We note that the results presented here provide the first experimental evidence—to our knowledge—for extremely large enhancements of radiative heat transfer in the extreme near field between both dielectric and metal surfaces. Furthermore, our results establish the fundamental validity of fluctuational electrodynamics in modelling eNFRHT and NFRHT. The technical advances described in this work are key to systematically investigating eNFRHT phenomena in a variety of materials and nanostructures, and provide critical information that complements insights that can be obtained by other near-field techniques[30,31]. Knowledge gained from such studies will be critical to the development of future technologies that leverage nanoscale radiative heat transfer[32].

1. Challener, W. A. *et al.* Heat-assisted magnetic recording by a near-field transducer with efficient optical energy transfer. *Nature Photon.* **3,** 220–224 (2009).
2. Basu, S., Zhang, Z. M. & Fu, C. J. Review of near-field thermal radiation and its application to energy conversion. *Int. J. Energy Res.* **33,** 1203–1232 (2009).
3. Pendry, J. B. Radiative exchange of heat between nanostructures. *J. Phys. Condens. Matter* **11,** 6621–6633 (1999).
4. Shen, S., Narayanaswamy, A. & Chen, G. Surface phonon polaritons mediated energy transfer between nanoscale gaps. *Nano Lett.* **9,** 2909–2913 (2009).
5. Rousseau, E. *et al.* Radiative heat transfer at the nanoscale. *Nature Photon.* **3,** 514–517 (2009).
6. Song, B. *et al.* Enhancement of near-field radiative heat transfer using polar dielectric thin films. *Nature Nanotechnol.* **10,** 253–258 (2015).
7. Kittel, A. *et al.* Near-field heat transfer in a scanning thermal microscope. *Phys. Rev. Lett.* **95,** 224301–224304 (2005).
8. Worbes, L., Hellmann, D. & Kittel, A. Enhanced near-field heat flow of a monolayer dielectric island. *Phys. Rev. Lett.* **110,** 134302 (2013).
9. Kim, K., Jeong, W., Lee, W. & Reddy, P. Ultra-high vacuum scanning thermal microscopy for nanometer resolution quantitative thermometry. *ACS Nano* **6,** 4248–4257 (2012).
10. Lee, W. *et al.* Heat dissipation in atomic-scale junctions. *Nature* **498,** 209–212 (2013).
11. Rytov, S. M. *Theory of Electric Fluctuations and Thermal Radiation* (Air Force Cambrige Research Center, 1953).
12. Joulain, K., Mulet, J.-P., Marquier, F., Carminati, R. & Greffet, J.-J. Surface electromagnetic waves thermally excited: radiative heat transfer, coherence properties and Casimir forces revisited in the near field. *Surf. Sci. Rep.* **57,** 59–112 (2005).
13. Rodriguez, A. W., Reid, M. T. H. & Johnson, S. G. Fluctuating-surface-current formulation of radiative heat transfer: theory and applications. *Phys. Rev. B* **88,** 054305 (2013).
14. Planck, M. & Masius, M. *The Theory of Heat Radiation* (P. Blakiston Son & Co, 1914).
15. Song, B., Fiorino, A., Meyhofer, E. & Reddy, P. Near-field radiative thermal transport: From theory to experiment. *AIP Adv.* **5,** 053503 (2015).
16. Rytov, S. M., Kravtsov, Y. A. & Tatarskii, V. I. *Principles of Statistical Radiophysics* (Springer, 1989).
17. Polder, D. & Hove, M. A. V. Theory of radiative heat transfer between closely spaced bodies. *Phys. Rev. B* **4,** 3303–3314 (1971).
18. Shen, S., Mavrokefalos, A., Sambegoro, P. & Chen, G. Nanoscale thermal radiation between two gold surfaces. *Appl. Phys. Lett.* **100,** 233114 (2012).
19. Altfeder, I., Voevodin, A. A. & Roy, A. K. Vacuum phonon tunneling. *Phys. Rev. Lett.* **105,** 166101 (2010).
20. Singer, F., Ezzahri, Y. & Joulain, K. Near field radiative heat transfer between two nonlocal dielectrics. *J. Quant. Spectrosc. Radiat. Transf.* **154,** 55–62 (2015).
21. Chiloyan, V., Garg, J., Esfarjani, K. & Chen, G. Transition from near-field thermal radiation to phonon heat conduction at sub-nanometre gaps. *Nature Commun.* **6,** 6755 (2015).
22. Kim, K. *et al.* Quantification of thermal and contact resistances of scanning thermal probes. *Appl. Phys. Lett.* **105,** 203107 (2014).
23. Wischnath, U. F., Welker, J., Munzel, M. & Kittel, A. The near-field scanning thermal microscope. *Rev. Sci. Instrum.* **79,** 073708 (2008).
24. Sadat, S., Meyhofer, E. & Reddy, P. Resistance thermometry-based picowatt-resolution heat-flow calorimeter. *Appl. Phys. Lett.* **102,** 163110–163113 (2013).
25. Rodriguez, A. W., Reid, M. T. H. & Johnson, S. G. Fluctuating-surface-current formulation of radiative heat transfer for arbitrary geometries. *Phys. Rev. B* **86,** 220302 (2012).
26. Reid, M. T. H. & Johnson, S. G. Efficient computation of power, force and torque in BEM scattering calculations. *IEEE Trans. Antenn. Propag.* **63,** 3588–3598 (2015).
27. Mulet, J. P., Joulain, K., Carminati, R. & Greffet, J. J. Enhanced radiative heat transfer at nanometric distances. *Microscale Therm. Eng.* **6,** 209–222 (2002).
28. Mulet, J. P., Joulain, K., Carminati, R. & Greffet, J. J. Nanoscale radiative heat transfer between a small particle and a plane surface. *Appl. Phys. Lett.* **78,** 2931–2933 (2001).
29. Chapuis, P. O., Volz, S., Henkel, C., Joulain, K. & Greffet, J. J. Effects of spatial dispersion in near-field radiative heat transfer between two parallel metallic surfaces. *Phys. Rev. B* **77,** 035431 (2008).
30. Jones, A. C. & Raschke, M. B. Thermal infrared near-field spectroscopy. *Nano Lett.* **12,** 1475–1481 (2012).
31. De Wilde, Y. *et al.* Thermal radiation scanning tunnelling microscopy. *Nature* **444,** 740–743 (2006).
32. Otey, C. R., Lau, W. T. & Fan, S. H. Thermal rectification through vacuum. *Phys. Rev. Lett.* **104,** 154301 (2010).

Supplementary Information is available in the online version of the paper.

Author Contributions The work was conceived by P.R., E.M., F.J.G.-V. and J.C.C. The experiments were performed by K.K., W.L., L.C. and B.S. under the supervision of E.M. and P.R. The devices were designed, fabricated and characterized by K.K., W.J., D.T. and B.S. Characterization of dielectric properties was performed by B.S. Modelling was performed by V.F.-H., J.F. and B.S. (with inputs from M.T.H.R.) under the supervision of F.J.G.-V. and J.C.C. The manuscript was written by J.C.C., E.M. and P.R. with comments and inputs from all authors.

Author Information Reprints and permissions information is available at www.nature.com/reprints. The authors declare no competing financial interests. Readers are welcome to comment on the online version of the paper. Correspondence and requests for materials should be addressed to J.C.C. (juancarlos.cuevas@uam.es) or E.M. (meyhofer@umich.edu) or P.R. (pramodr@umich.edu).

1. Fabrication of Scanning Probes and Suspended Microdevices

The scanning thermal microscopy (SThM) probes required for this work were custom-fabricated. Fabrication of the SThM probes follows the basic approach outlined in our previous work[9] on nanoscale-resolution scanning probe thermometry. All SThM probes feature a Au-Cr thermocouple that is integrated into the distal end of the probe's tip. Upon fabrication of the basic probe, subsamples were specifically modified to enable the experiments presented in this work. Probes with dielectric surface materials were coated with SiO_2 or SiN by depositing 100 nm of PECVD SiO_2 or SiN (non-stoichiometric), respectively, on pristine SThM probes. Au-coated probes were prepared by first depositing 100 nm of PECVD SiN on the SThM probes, followed by a 30 nm layer of Au deposited by electron-beam (e-beam) evaporation. The role of the SiN layer is to electrically isolate the outer Au layer from the Cr layer of the thermocouple. Scanning electron microscope images of the probes, obtained after using them in our experiments, are shown in Figs. S1, S2 & S3.

The key steps for fabricating the suspended microdevices, used in high-resolution Au-Au eNFRHT measurements, are shown in Fig. S4. Briefly, the device is made from a Silicon-On-Insulator (SOI) wafer that has a 500 µm-thick Si substrate, a 1 µm-thick buried oxide (BOX) layer and a 10 µm-thick Si device layer (Step 1). A 500 nm-thick, low stress LPCVD SiN (non-stoichiometric) film is first deposited on the wafer for electrical insulation of subsequent metal patterns on the device layer (Step 2), followed by the deposition of a 2 µm-thick layer of low-temperature LPCVD SiO_2 (Step 3). A 100 nm-thick layer of Au is deposited on the SiO_2 layer using e-beam evaporation (Step 4). Using the same mask, the Au layer is etched followed by the etching of the SiO_2 layer using reactive-ion etching (RIE), leaving a square pad from which Au-Au eNFRHT measurements are subsequently made (Step 5). A Pt resistance heater-thermometer with its electrical connections is then patterned on the SiN layer using successive lift-off processes (Step 6). The device profile is formed by RIE through the SiN layer and the Si device layer from the front side of the wafer, stopping at the BOX layer (Step 7). Subsequently, the SiN layer and the SiO_2 layer on the back of the wafer are selectively etched using RIE to open a window for further processing (Step 8). The device is suspended by etching through the Si substrate from the backside using deep reactive-ion etching, stopping at the BOX layer (Step 9). Finally, the BOX layer is removed using a buffered hydrofluoric acid (BHF) etch (Step 10).
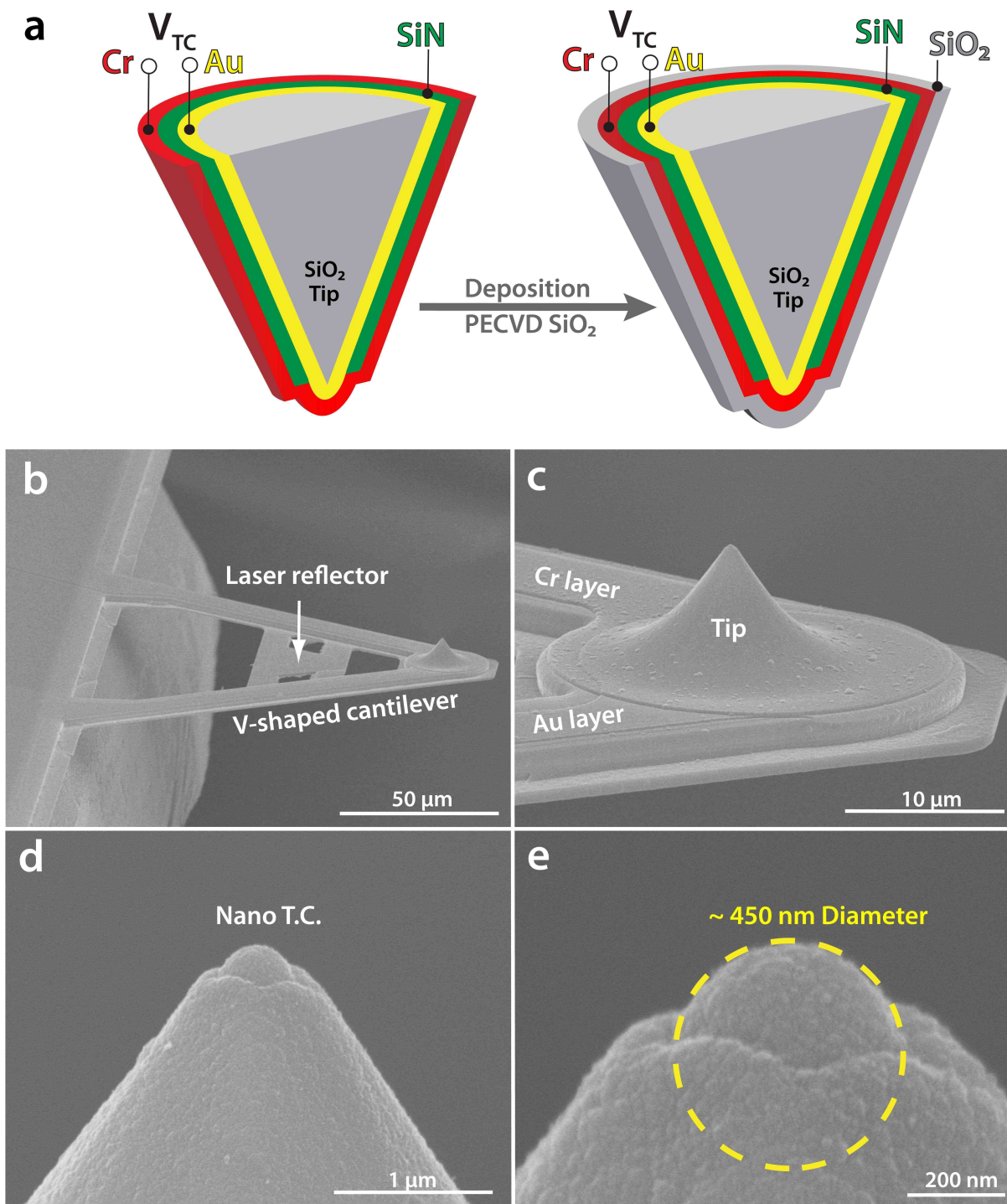
Figure S1. Schematic cross-section of the tip of the probe and Scanning Electron Microscope (SEM) images of the SiO₂ coated scanning probe used in our experiments. a, Schematic cross-section of the SiO_2-coated tip. **b-d,** SEM images of the fabricated probes. The cantilevered scanning thermal probe (**b**), the tip with the metallic Au and Cr wires (**c**), a magnified view of the tip (**d**) and the tip's apex with the spherical thermocouple portion (**e**) are shown. Images as shown in (**e**) were used to estimate the tip diameter (~450 nm).
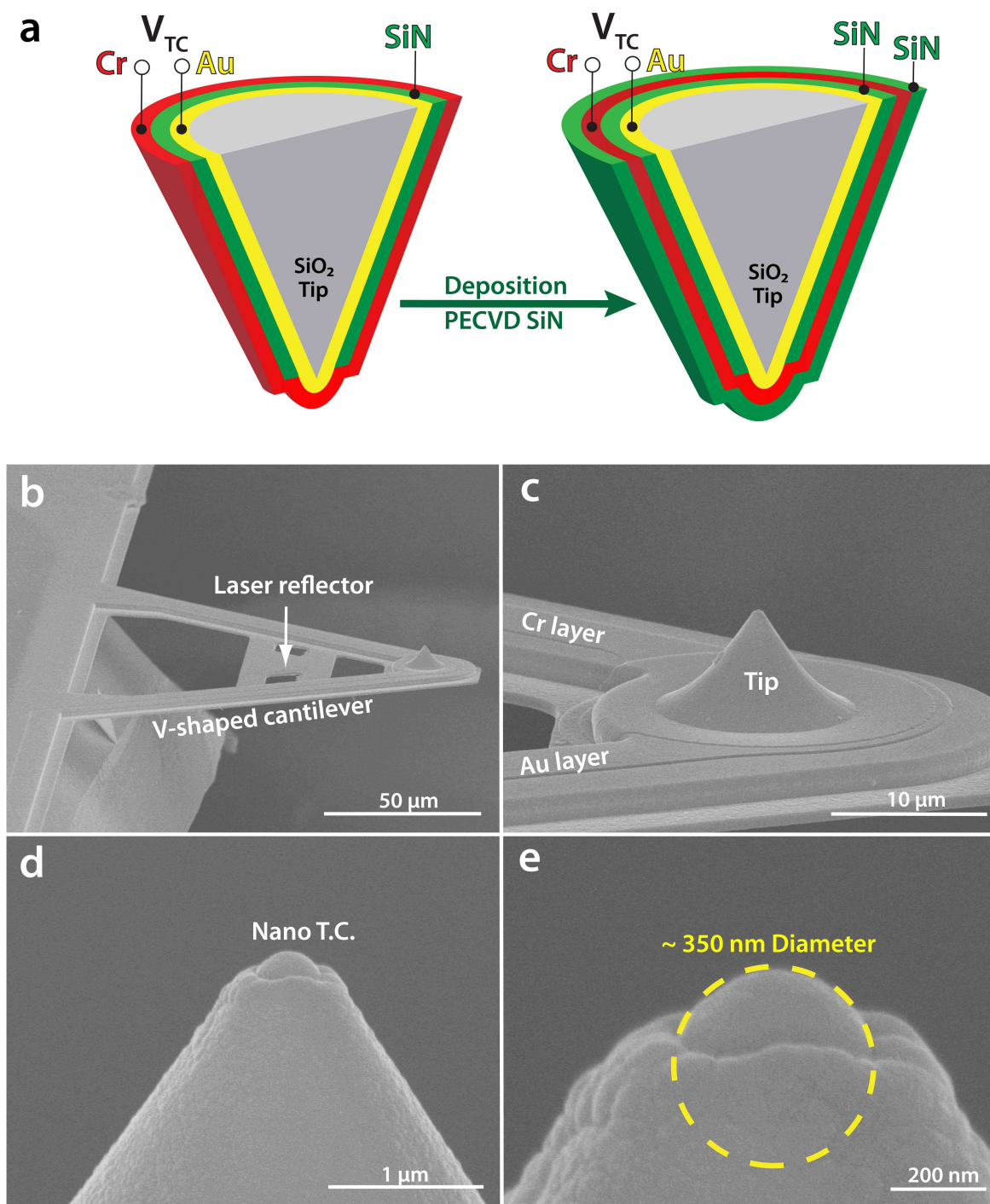
Figure S2. Schematic cross-section of the tip of the probe and SEM images of the SiN-coated scanning probe used in our experiments. a, Schematic describing the cross-section of the SiN coated tip. **b-d,** SEM images of the fabricated devices. The cantilevered scanning thermal probe (**b**), the tip (**c**), a zoomed image of the tip (**d**), and the apex, which contains the spherical portion of the tip (**e**), are shown. From the image shown in (**e**) the tip diameter was estimated to be ~350 nm.
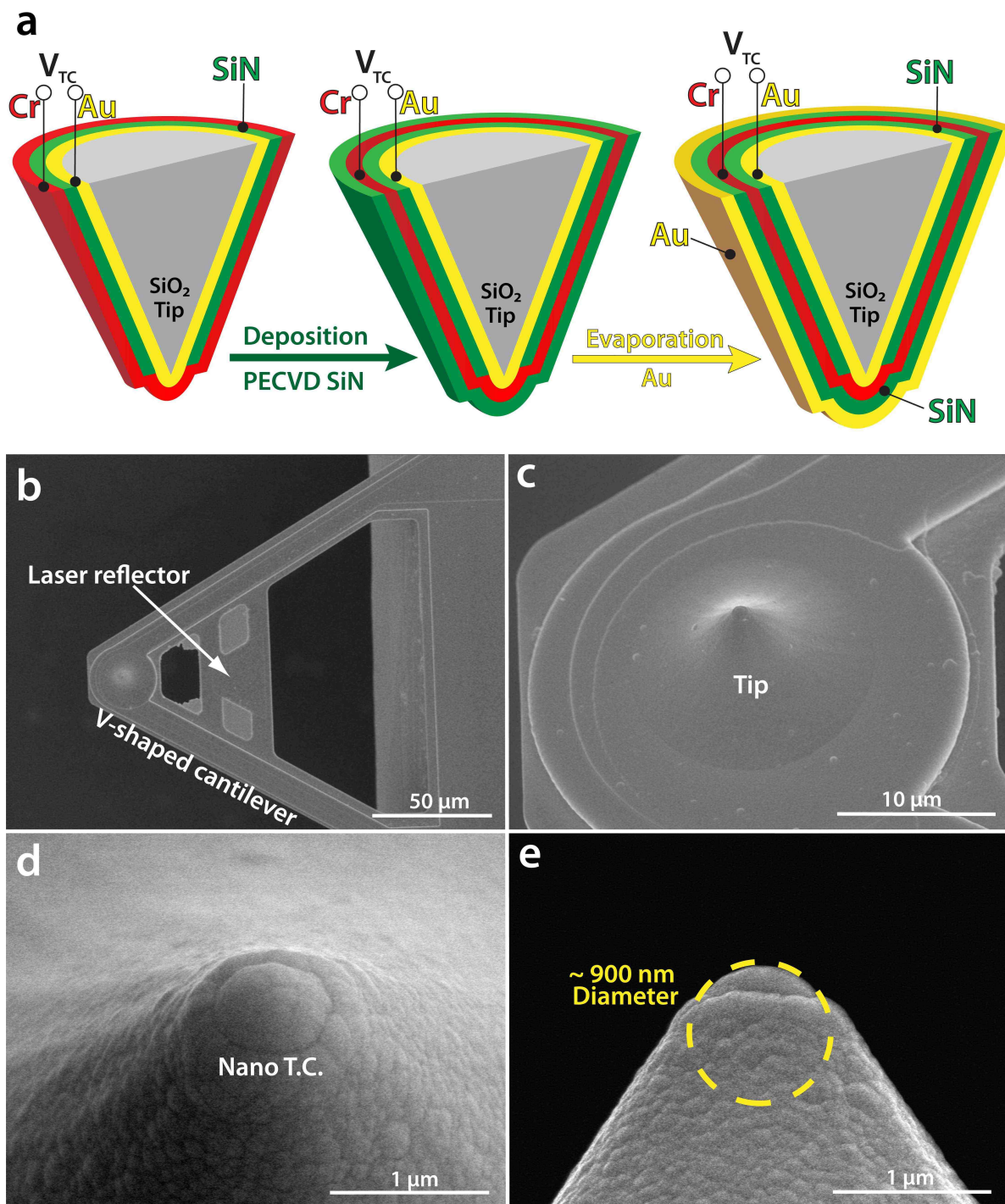
Figure S3. Schematic cross-section of the tip of the probe and SEM images of the Au-coated scanning probe used in our experiments. a, Schematic describing the cross-section of the Au-coated tip. **b-d,** SEM images of the fabricated devices. The cantilevered scanning thermal probe (**b**), the tip (**c**), a zoomed image of the tip (**d**), and the apex, which contains the spherical portion of the tip (**e**), are shown. From the image shown in (**e**) the tip diameter was estimated to be ~900 nm.
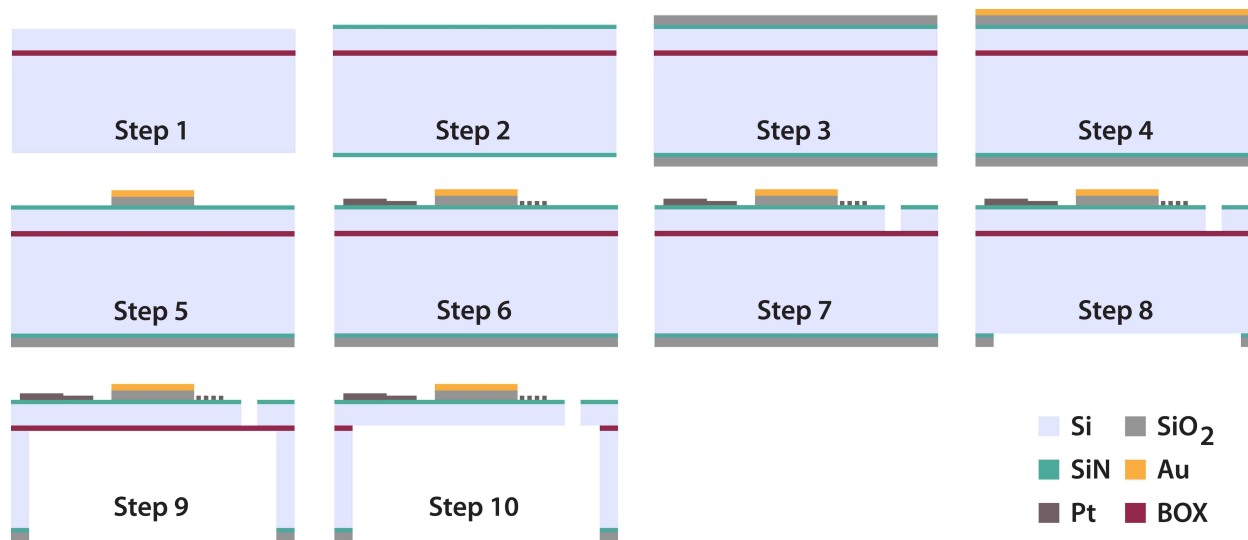
Figure S4. Schematic describing the steps in the fabrication of the suspended microdevice. Step 1, SOI wafer, where the buried oxide layer (BOX) is shown. Step 2, deposition of a SiN insulator. Step 3, deposition of LPCVD oxide. Step 4, Au deposition. Step 5, patterning of Au and oxide. Step 6, patterning of Pt resistance thermometer and electrical connections. Step 7, RIE to form the device profile. Step 8, backside etching via RIE. Step 9, DRIE to suspend the device. Step 10, removal of the BOX layer via a BHF etch. Additional details regarding this microdevice fabrication can be found in section 1 of the SI.

2. Substrate Preparation

In order to prepare the dielectric substrates used in the experiments we deposited 100 nm of silicon dioxide (SiO_2) or silicon nitride (SiN) on silicon substrates (PECVD). From atomic force microscopy (AFM) analysis the RMS roughness of the SiO_2 and SiN surfaces was found to be 0.2 nm and 0.4 nm, respectively (see Fig. S5a & b for AFM images). In estimating this RMS roughness we used data from 200 nm × 200 nm AFM scans: These dimensions were chosen because they were large enough to represent the area over which eNFRHT measurements were taken. The Au-coated substrates used in the experiments were prepared by deposition of 100 nm of Au on mica using e-beam evaporation. The RMS roughness of the samples prepared using this approach is 0.5 nm. Finally, the RMS roughness of the Au layer (100 nm thick) on the suspended microdevice was also characterized using AFM and found to be ~0.9 nm. Since the surface roughness of all the devices used in our experiments was substantially smaller than that of the probes, the roughness of the surfaces was considered negligible in all our computational analysis.
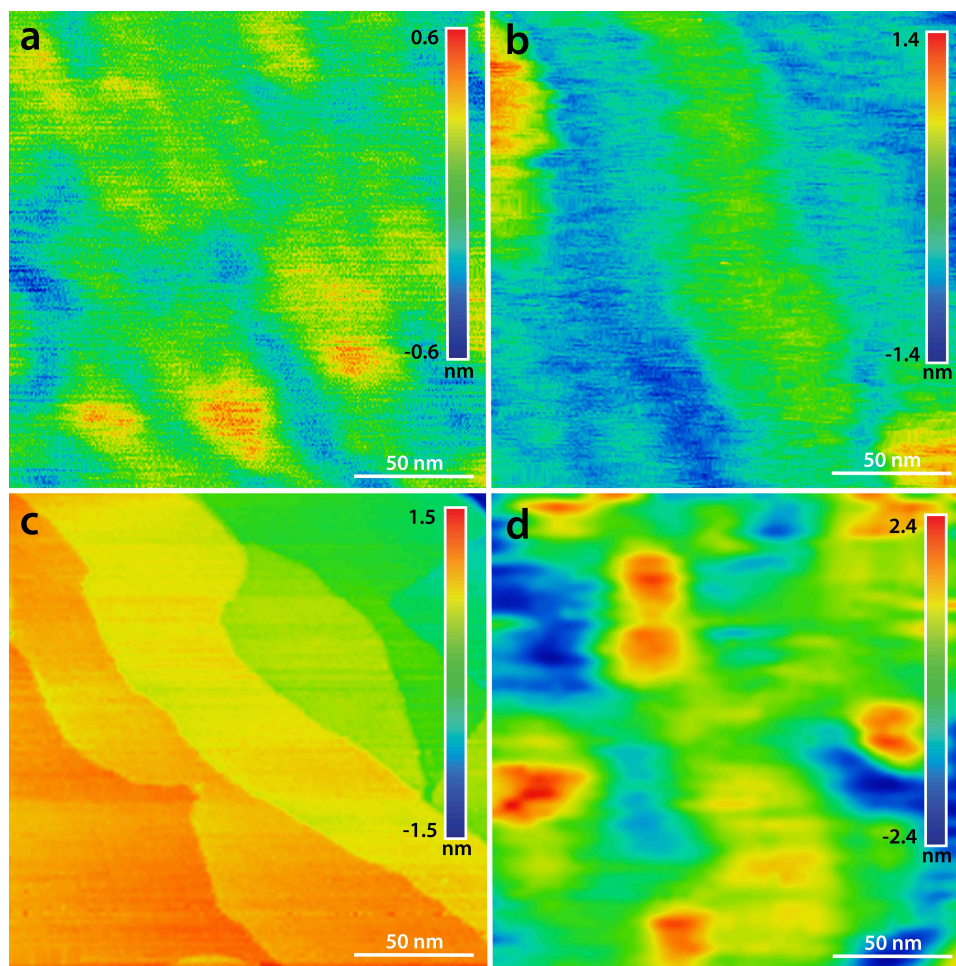
Figure S5. Atomic force microscopy images of surface roughness. a, Surface topography of a 100 nm-thick SiO_2 film deposited on a Si substrate (RMS roughness 0.15 nm). **b**, Surface topography of a 100 nm thick SiN film deposited on a Si substrate (RMS roughness 0.4 nm). **c,** Surface topography of a 100 nm thick Au film deposited on mica (RMS roughness 0.5 nm). **d,** Surface topography of a 100 nm thick Au deposited on the suspended microdevice (RMS roughness 0.9 nm). All the scanning areas are 200 nm × 200 nm in size.

3. Ultra-Low Noise Measurement Environment

The experiments described in this work were performed in a UHV-scanning probe instrument housed in an ultra-low noise facility where the ground vibrations were attenuated to meet the stringent NIST-A criterion[33]. The temperature of the facility was controlled to vary <0.1 K about a chosen set point (294 K). The acoustic noise in the measurement chamber in which our scanning probe microscope is operated, is below 30 dB SPL (sound pressure level in dB with respect to a 20 µPa reference level) in the frequency range from 60 – 100 Hz, and declines

monotonically from this value with increasing frequency throughout the entire acoustic range. At 1 kHz, for example, the SPL decreases to ~ -15 dB.

4. Displacement of the SThM Probe Towards Heated Substrate and Measurement of Thermoelectric Voltage Output

In unmodulated experiments the SThM probe was displaced towards the heated substrate at a rate of 0.5 nm/s, and the thermoelectric voltage output from the SThM probe was measured in a bandwidth of 5 Hz. In modulated measurements the temperature of the microdevice was modulated by 5 K at 18 Hz when the gap size was larger than 6 nm. At smaller gap sizes the amplitude was reduced to 2.5 K to attenuate mechanical deflections from bimaterial effects to <0.3 nm (see section 11). The gap size in the unmodulated measurements was referenced to the point at which snap-in occurs. This was found to be adequate for accurately quantifying gap size as the mechanical drift in the experiments during the time of the measurement (100 s) was negligibly small (~0.1 nm). However, in the modulated experiments it took ~1000 s to acquire each data point in Fig. 3d of the mansucript, necessitating measurements that lasted over 12 hours in total during which drift is significant. Therefore, we performed individual gap size calibrations for each data point (*i.e.* every 1000 s period) by displacing the probe towards the microdevice until contact was made. This enabled direct measurements of the gap size for each data point shown in Fig. 3d. In all experiments, the measured thermoelectric voltages were related to the temperature rise via the calibrated[9] Seebeck coefficient (16.3 μV/K) of the Au-Cr junction.

5. Quantification of the Distance at which Snap-in Occurs

Snap-in is a sudden contact between the tip and the substrate, which takes place when the tip at the end of the SThM cantilever, is brought into close proximity (maximally a few nanometers or less) of a (planar) surface/substrate. Snap-in occurs primarily due to instabilities that arise from electrostatic and near-field forces that have a non-linear distance dependence. Snap-in limits the smallest gaps at which we are able to perform eNFRHT measurements.

The snap-in distance was quantified using approaches developed in the past in the field of scanning probe microscopy[34]. Briefly, we performed experiments where we monitored the deflection of the cantilever using an optical scheme when the gap size between the tip and the

substrate was systematically reduced. Figure S6 presents a representative trace of the deflection signal (photodiode signal) from one such experiment. As illustrated in the insets of the figure, the cantilevered portion of the probe is initially in an unbent state. When the probe snaps-in the cantilever bends downwards due to the attractive forces between the tip and the substrate. Upon further displacement of the probe, the cantilever is returned to its "unbent state". The additional displacement required to reach this unbent state represents the snap-in distance as indicated in Fig. S6. From measurements like these, the snap-in distance in experiments with SiO_2, SiN and Au probes (where the temperature was not modulated) was estimated to be 1.9 ± 0.4 nm, 2.4 ± 0.3 nm, 2.2 ± 0.5 nm, respectively. The snap-in distance for modulated Au-Au measurements was similarly estimated to be 2.8 ± 0.2 nm.
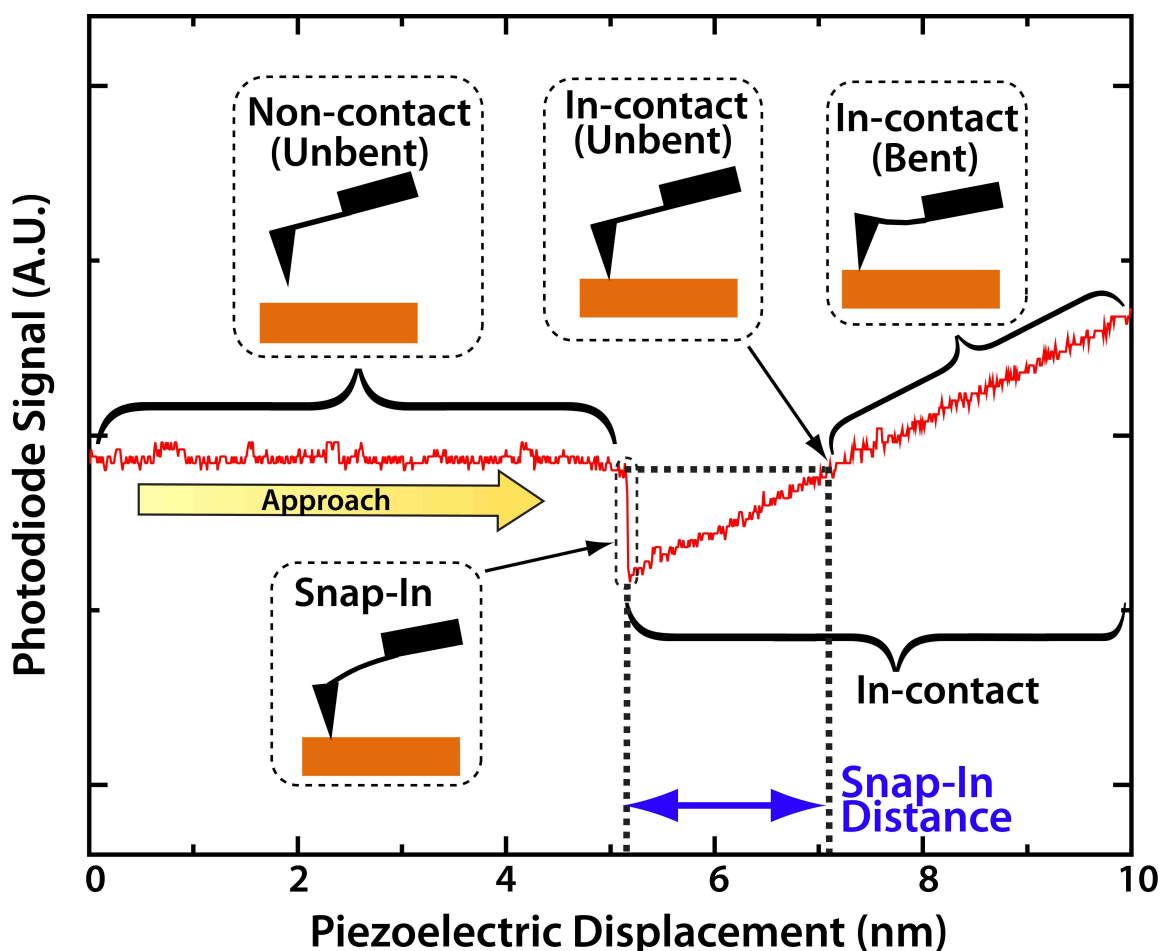

Figure S6. Quantification of snap-in distance. A typical trace showing the deflection of the cantilever of the probe as it is displaced towards the substrate. Cantilever deflection is measured via an optical signal that is quantified by a photodiode detector (not shown).
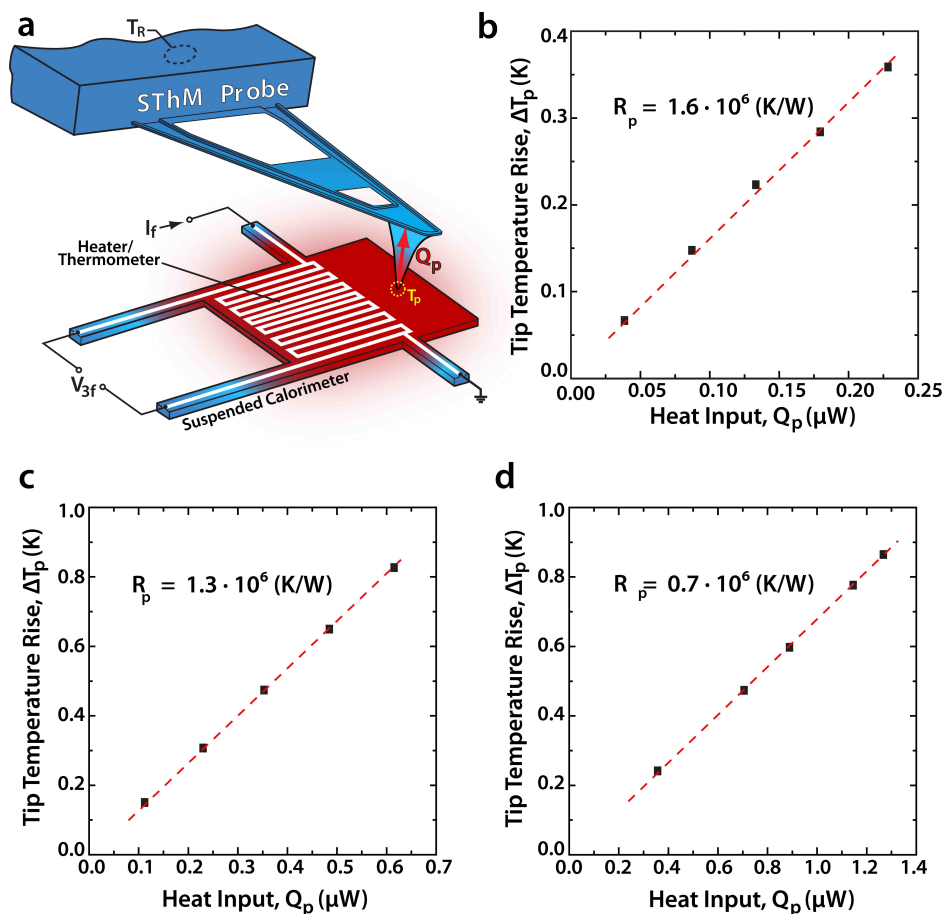
Figure S7. Measurement of thermal resistance of the SThM probes. a. Schematic of the measurement approach employed to determine the thermal resistance of the probes. **b-d,** Measured tip temperature rise ($\Delta T_P = T_P - T_R$) as a function of the heat current (Q_P) for SiO_2 (**b**), SiN (**c**) and Au (**d**) coated probes. Insets show the measured thermal resistance (R_P).

6. Thermal Resistance Measurements of Scanning Probes

In order to experimentally measure the thermal resistance of the SThM probes we followed a procedure similar to that described in recent work from our group[22]. Briefly, we employed suspended calorimeters (Fig. S7a) with embedded platinum heater-thermometers and input known quantities of heat into the suspended region. This resulted in a temperature rise that could be accurately measured using the embedded platinum thermometers. Subsequently, we placed each of the SThM probes used in the experiments in contact with the heated suspended calorimeter (at a pre-determined contact force). This resulted in heat loss through the point-contact between the tip and the calorimeter that in turn is reflected as a lower temperature rise of

the calorimeter. The decrease in the temperature of the calorimeter was again quantified via the Pt thermometer. The difference in the measured temperatures before and after contact formation enabled us to determine the heat flow/input (Q_P) through the SThM probe. Further, using the thermocouple embedded in the tip of the SThM probe we also simultaneously measured the temperature rise (ΔT_P) of the tip upon contacting the calorimeter. This enabled us to readily determine the thermal resistance (R_P) of the SThM probe using: $R_P = \Delta T_P / Q_P$. Figures S7b, c & d show the measured temperature rise of SiO_2, SiN and Au coated probes, respectively, as a function of Q_P. From these data the thermal resistance of the probes (R_P) was readily obtained and is shown in the insets of Fig. S7b, c & d. Please see Ref. 22 for more details of this thermal resistance measurement scheme.

7. Noise Characterization of Thermoelectric Voltage of SThM Probes

The thermoelectric voltage output from the thermocouple embedded in the SThM probe has noise contributions from Johnson noise, low frequency temperature drift and other sources. This noise was quantified by computing the power spectral density (PSD, Fig. S8) of the output from the thermocouple using a SR760 FFT analyzer from Stanford Research Systems. The signal was first amplified using a two stage custom built amplifier with a gain of 10^4 prior to signal processing. The measured PSD in Fig. S8 clearly shows that at low frequencies noise increases rapidly with decreasing frequency. In unmodulated measurements which employ a bandwidth of 5 Hz, the noise-limited temperature resolution is estimated to be ~15 mK. It can also be seen that the temperature resolution is greatly improved when modulated measurements are performed at a frequency above 10 Hz (where the noise spectrum becomes flat). Specifically, if the temperature of the hot substrate is modulated at 18 Hz and the thermoelectric voltage is measured in a bandwidth of 0.8 mHz, the temperature resolution (ΔT_{Res}) can be as high as ~20 μK. Once the temperature resolution is known, the corresponding heat flow resolution (Q_{Res}) is obtained via $Q_{\text{Res}} = \Delta T_{\text{Res}} / R_P$. For the Au-coated probes which have a resistance of $R_p = 0.7 \times 10^6$ K/W, an unmodulated temperature measurement results in a heat flow resolution of ~22 nW, while a resolution as high as 30 pW can be achieved with 18 Hz temperature modulation. Further, since the gap thermal conductance is given as the ratio between heat flow and its driving temperature difference, one can also estimate the thermal conductance resolution. Specifically, a thermal

conductance as small as 220 pW/K can be detected when an unmodulated temperature differential of ~100 K is applied, whereas thermal conductances as small as 6 pW/K can be detected when modulated temperature differentials of ~5 K are applied.
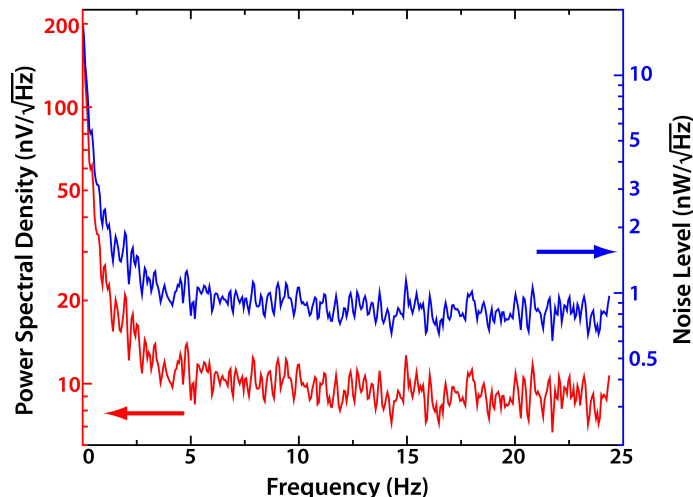

Figure S8. Noise characteristics of the probe thermoelectric voltage signal (referenced to the input). Measured PSD of the thermoelectric voltage output from a Au-coated probe. The red plot shows the PSD in nV/Hz$^{1/2}$, whereas the blue line presents the PSD in units of nW/Hz$^{1/2}$.

8. Modulation of the Temperature of the Microdevice and Measurement of the Amplitude of Temperature Modulation

The microdevice temperature was modulated sinusoidally (18 Hz) at an amplitude of 5 K by supplying a sinusoidal electric current (amplitude 0.49 mA, frequency 9 Hz) into the serpentine Pt line integrated into the microdevice. A correspondingly smaller current (0.35 mA) was applied in measurements at smaller gaps, which employed a 2.5 K temperature differential. All temperature oscillations were quantified by measuring the voltage oscillations at $3f$ = 27 Hz across the Pt line as described in our previous work[24].

9. Frequency Response of the Suspended Microfabricated Devices and the SThM Probes

The frequency response of the suspended microdevice was characterized following an approach described in our previous work on calorimetry[24]. Briefly, we systematically increased the frequency (f) of the sinusoidal electric current input into the integrated resistance heater-thermometers embedded into the microdevice while maintaining a constant amplitude (400 μA).

The temperature fluctuations of the device at $2f$ were measured by monitoring the voltage fluctuation at $3f$.

Figure S9a shows the normalized amplitude of temperature oscillations as a function of the frequency of temperature oscillations ($2f$) for the suspended microdevice. It can be seen that the temperature response is relatively constant up to a frequency of 20 Hz, clearly showing that temperature can be readily modulated at frequencies below this cut-off. In order to measure the thermal frequency response of the SThM probe we focused a laser beam at the very end of the cantilevered portion of the probe and modulated the laser power sinusoidally at a range of frequencies while maintaining a constant amplitude. The oscillating tip temperature was then recorded via the embedded thermocouple. Figure S9b shows that the measured frequency response of the probe remains flat until a heating frequency of about 10 Hz and drops by ~13% at 18 Hz, which was systematically accounted for in our data analysis.
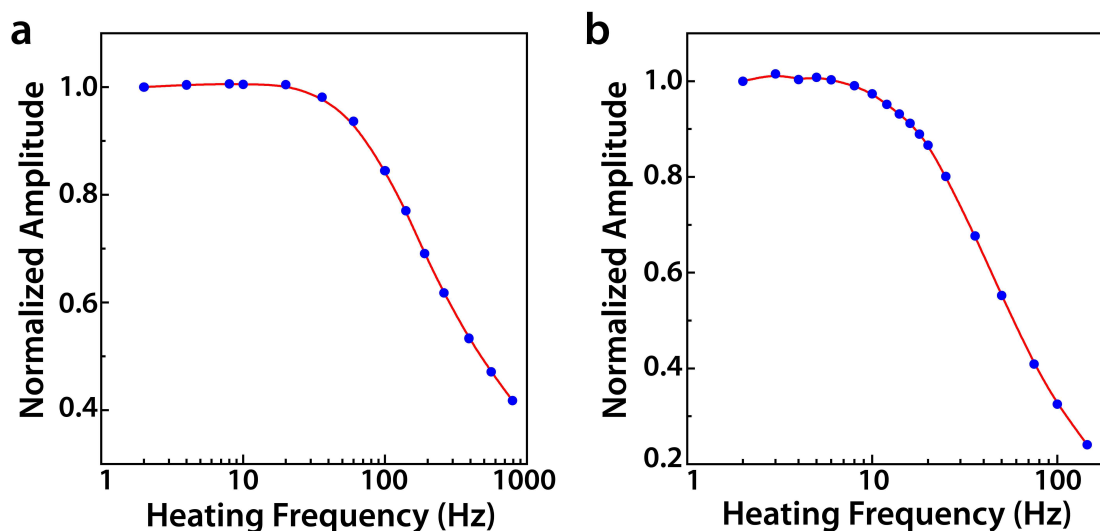

Figure S9. Frequency response of the suspended microdevice and the SThM probes. Normalized amplitude of temperature oscillations as a function of frequency for the microdevice (**a**) and the Au-coated SThM probe (**b**). The amplitudes of temperature oscillations were normalized to peak values, which occur at the lowest measurement frequency.

10. Characterization of the Thermal Conductance of Suspended Microdevices

The thermal conductance of the suspended microdevices was characterized using an approach similar to that described in our previous work on picowatt resolution calorimetry[24]. In order to measure the thermal conductance we input known amounts of heat into the suspended region of the device and measured the corresponding temperature rise. The relationship between the power

input (Q_{in}) and the measured temperature rise (ΔT) is shown in Fig. S10 and can be used to readily estimate the thermal conductance of the beams of the device (G_{beams}) via $G_{beams} = Q_{in} / \Delta T$, which is about 175 µW/K. Please see ref. 24 for more details on the scheme used for characterization of the thermal conductance.
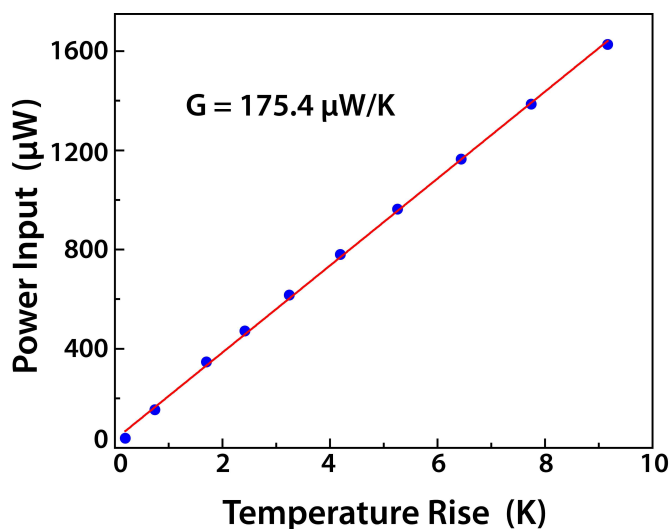

Figure S10. Thermal conductance of the suspended microdevice. The relationship between the temperature rise of the suspended region and the power dissipated is given (experiments were performed in UHV conditions to eliminate contributions from conduction through air). The slope of the plotted line represents the conductance of the beams of the suspended microdevice.

11. Characterization of the Thermally-Induced Deflections of Suspended Microdevices

Sinusoidal heating of the suspended microdevice results in both periodic temperature oscillations as well as thermally induced mechanical deflections of the suspended region due to bimaterial effects. These mechanical oscillations, if large, can potentially impact the smallest gap sizes that can be achieved between the tip and the suspended device. In order to quantify these thermally induced deflections we first placed a SThM probe in good mechanical contact (contact force of ~150 nN) with the suspended device. The laser light reflecting off the probe (see Fig. 1) into a quadrant photodiode provides the feedback signal to a control loop (control loop bandwidth > 1 kHz). The control loop supplies a feedback voltage to the piezoelectric tube onto which the SThM probe is mounted and acts to displace the piezoelectric tube and the SThM probe by an amount equal to the deflection of the microdevice so as to maintain a constant probe deflection. Figure S11 shows the displacement of the piezoelectric tube when the microdevice temperature

was modulated by 12 K at 18 Hz. It can be seen that the amplitude of the displacement is ~1.5 nm, which in turn implies that the sensitivity is ~0.12 nm/K (=1.5 nm/12 K). Data obtained at lower temperature modulations (not shown) indeed confirms this result. We note that in our experiments, the amplitude of temperature oscillations employed for measurements in small gaps (<6 nm) is limited to 2.5 K. This corresponds to mechanical oscillations of amplitude ~0.3 nm which are significantly smaller than the snap-in distance (~3 nm) observed in the modulated Au-Au measurements. Hence the effect of mechanical oscillations is negligible.
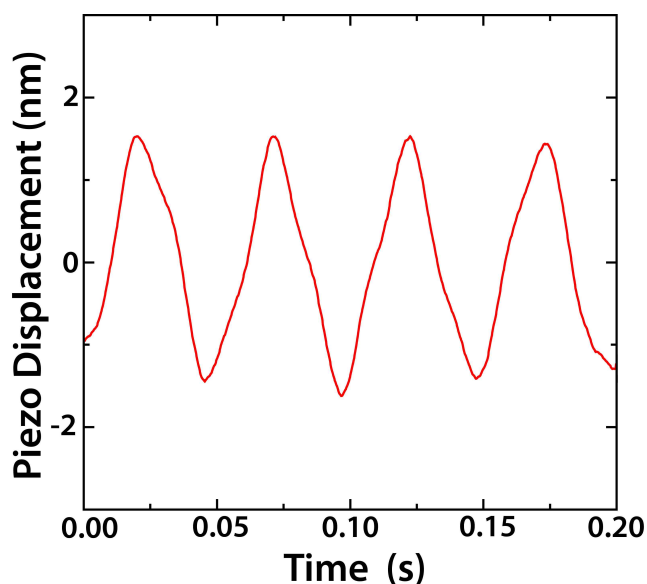

Figure S11. Characterization of the thermally induced mechanical deflections of suspended microdevices. The measured piezoelectric displacement under feedback control, when the temperature of the microdevice was sinusoidally (18 Hz) modulated by 12 K. From this data it can be readily inferred that the amplitude of deflection of the microdevice is ~0.12 nm/K.

12. Measured Dielectric Properties of Silicon Nitride

Modelling of near-field radiative heat transfer requires the frequency-dependent complex dielectric function of materials as a key input. It is well-known that even for nominally identical materials, the dielectric functions may differ due to variations in actual material compositions and microstructures as a function of preparation methods and conditions. The use of different dielectric functions for the same nominal material could lead to significant discrepancies among calculated near-field heat fluxes, analogous to what has been reported in the case of Casimir force[35] calculations.

While there is relatively little uncertainty in the composition of SiO_2 and Au films the stoichiometry of SiN films is sensitive to deposition conditions. Hence the frequency-dependent complex dielectric function of the SiN films deposited on the substrates used in our measurements was characterized using two Woollam[TM] spectroscopic ellipsometers (VUV-VASE and IR-VASE). Three angles of incidence (55°, 65° and 75°) were used and a wavelength range from 137 nm to 40 μm was covered. These measurements were performed to accurately account for the fact that the properties (porosity, chemical composition, dielectric function, etc.) of SiN films could vary significantly with different deposition methods and parameters. The dielectric function obtained from these measurements and subsequent analysis[36] is shown in Fig. S12b.
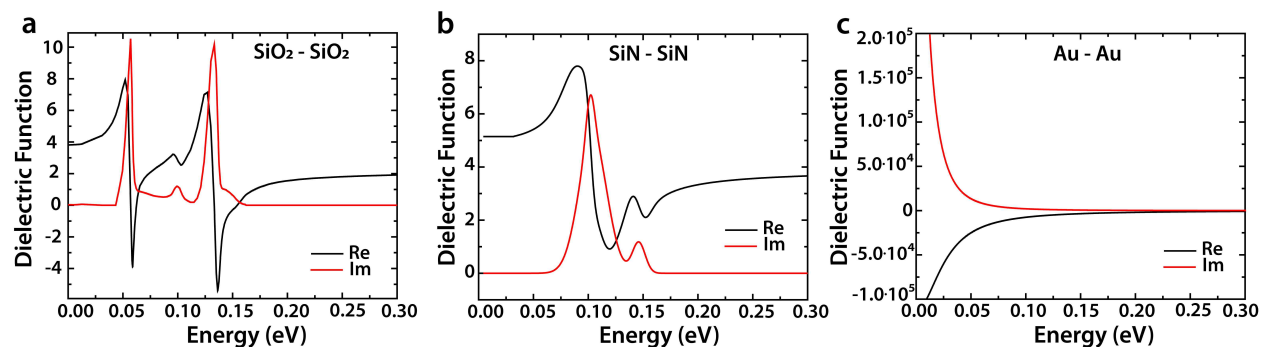

Figure S12. Dielectric functions. a-c, Real and imaginary parts of the dielectric functions employed in our simulations as a function of energy for SiO_2, SiN, and Au.

13. Formalism Employed for Computing Radiative Heat Transfer

In order to model the radiative heat transfer for the configurations experimentally studied by us we employed the fluctuating-surface-current (FSC) formulation of the heat transfer problem that has been recently put forward by one of us in collaboration with others[13,25]. This novel approach is based on the surface-integral-equation (SIE) formulation of classical electromagnetism and allows direct application of the boundary element method (BEM). In this method the electromagnetic scattering problem is solved by considering a set of linear equations involving a number of surface unknowns (fictitious surface currents in the surfaces of the objects). The FSC-BEM combination allows describing the radiative heat transfer between bodies of arbitrary shape, and can provide numerically exact results within the framework of fluctuational electrodynamics. In practice, we use the implementation of this approach provided in the open-source SCUFF-EM

software package[26,37] which was developed by one of us. This code makes use of the BEM to discretize the surfaces of the bodies into triangular elements or panels and the surface currents in each element are described by piecewise low-degree polynomials. In particular, SCUFF-EM employs the so-called RWG[38] basis of vector-valued polynomial functions defined on a mesh of triangular panels. This basis is suitable to deal with arbitrary geometries and yields results that converge with increasing resolution (smaller triangles). Further technical details can be found in refs. 13 and 25.

In our theoretical approach we assume that the radiative heat transfer can be well described in terms of dielectric functions that only depend on frequency or energy (local approximation). For our calculations we took the dielectric function of SiO_2 and Au from Palik[39], and Ordal *et al.*[40], respectively. The dielectric function for SiN was characterized by us as described in section 12 above. All dielectric functions used in this work are shown in Fig. S12 for the energy range relevant for heat transfer in our experiments.

14. Tip-Substrate Geometries and Convergence of Simulations

In order to provide a quantitative description of our experiments, we considered tip-substrate geometries like the one shown in Fig. S13a. The tip has a conical shape and ends in a spherical cap. The angle of the cone and the radius of the spherical cap have been obtained in every case from the SEM images of the experimental probes. For the cases discussed in the manuscript the tip radii were 450 nm for Au, 225 nm for SiO_2, and 175 nm for SiN. The height of the tip was chosen to be 3 μm for Au and 1.3 μm for SiO_2 and SiN. The substrate was modelled by a finite disk of radius 4 μm for Au and 2 μm for SiO_2 and SiN, and thickness 2 μm for Au and 1 μm for SiO_2 and SiN. The dimensions of both the tip and the substrate were carefully chosen so that there are no finite-size effects. Moreover, as explained in the manuscript, we have also simulated the roughness of our probes by including random Gaussian-correlated noise in the tip profile. To be precise, the maximum protrusion height on the tip of the probes was chosen to be 10 nm, and the correlation length between protrusions was chosen to be 17 nm.

A key issue in our numerical simulations is the choice of the mesh of triangular panels for the RWG-BEM approach. To obtain accurate results, the size of the triangular panels must be comparable to the (local) gap size or smaller. This was accomplished by employing a non-uniform grid that was finer at both the tip apex and in the centre of the plate (Fig. S13a).
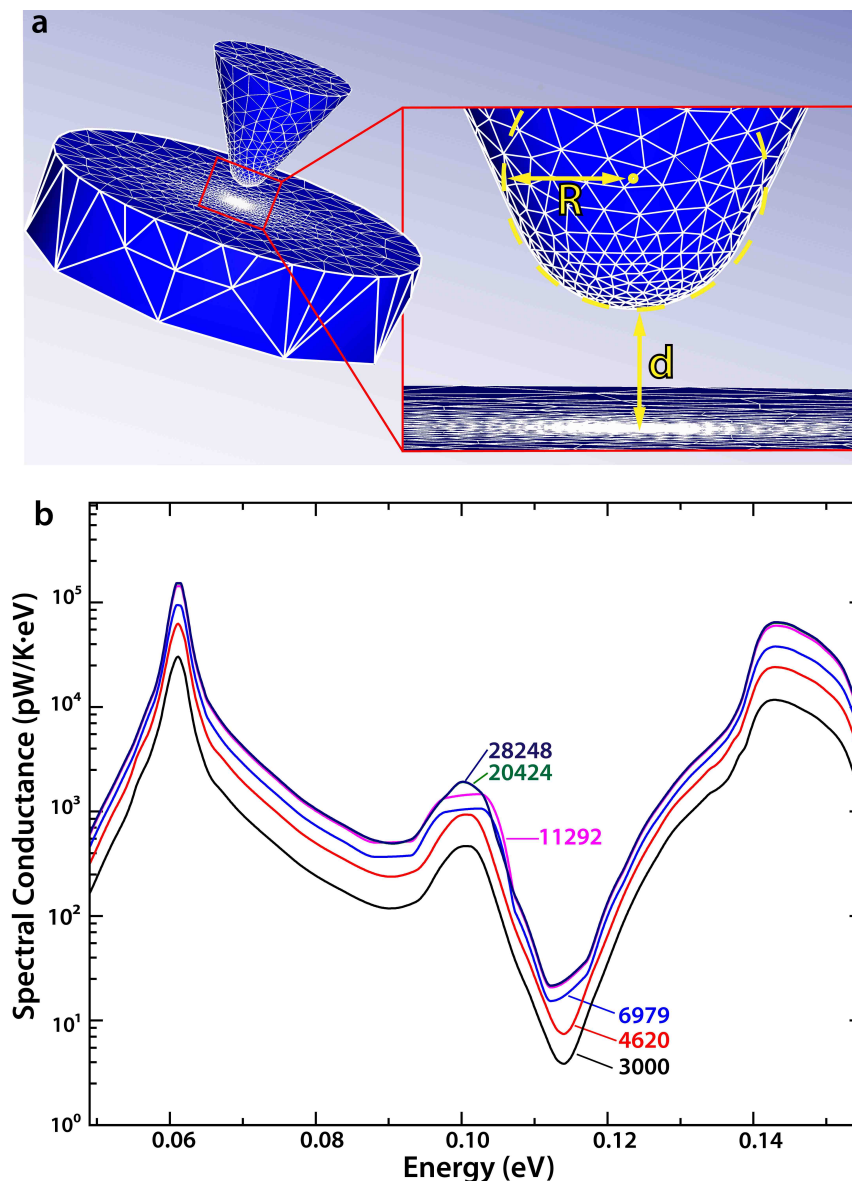
Figure S13. Simulated tip-substrate geometry and numerical convergence. a, Example of the tip-substrate geometries employed in our numerical simulations. The tip has a conical shape and ends in a spherical cap, while the substrate is modelled as a thick disk. The solid white lines correspond to the mesh of triangular panels used in the BEM calculations. The right inset shows a blow-up of the tip apex region. Here, R is the tip radius, and d is the gap size (or distance between the tip and the substrate). **b,** Example of a convergence test of the numerical results upon refinement of the mesh of triangular panels for a SiO_2 tip-substrate geometry with a tip radius of 200 nm and a gap size of 4 nm. In this case, the tip was assumed to not have any roughness. The different curves correspond to different numbers of basis functions employed in the BEM calculations as indicated in the figure. Notice that the two curves for the largest numbers of basis functions lie on top of each other illustrating the excellent convergence of our results. The reservoir temperatures in this calculation were assumed to be 310 K for the tip and 425 K for the substrate.

The convergence of our results was checked, for every combination of materials and every tip-substrate distance, by progressively refining the mesh, *i.e.* by reducing the size of the triangles and increasing the number of basis functions in the BEM calculations. In Fig. S13b we show an example of our convergence tests for the case of a SiO_2 tip-substrate geometry. It can be seen that the results progressively converge to a single solution (or spectral conductance) as the number of basis functions is increased. For calculations that included the presence of tip roughness, we have defined a smaller spherical cap around the tip apex where the triangular panels were chosen to have an equal size. The same was done in the substrate for a circular region around its centre. Again, the size of these triangles was checked to be sufficiently small to obtain converged results. We note that the convergence of the results with the size and the number of triangles depends on the material of choice. For metals (Au) the convergence is faster than for polar dielectrics (SiN, SiO_2) due to the different physical mechanism that dominates the NFRHT. In metals, NFRHT is governed by total internally reflected waves and does not depend critically on the distance between the tip and the plate. In contrast, NFRHT in polar dielectrics is dominated by surface phonon polaritons (SPhPs), electromagnetic waves whose dispersion relation is very sensitive to the distance between the two objects. Thus, the simulations for polar dielectrics require much more refined grids with considerably higher number of basis functions, *i.e.* with much smaller triangular panels.

15. Spectral Calculations of eNFRHT for SiN Gaps

For completeness, we report here the results for SiN that were not included in the manuscript. In particular, we show in Fig. S14a the spectral heat conductance for a SiN tip-substrate geometry for three different gap sizes. As one can see, the major contribution to heat transfer comes from an energy region around 0.12 eV, which corresponds to the energy of the transverse optical phonons in this material. As in the case of SiO_2, the coupling of optical phonons to electromagnetic waves gives rise to SPhPs that dominate the NFRHT. For this reason, the NFRHT rapidly decays with the gap size, very much like in the SiO_2 case and at odds with the Au case. An important conceptual difference between SiO_2 and SiN is that for SiN the real part of the dielectric constant never becomes negative, see Fig. S12. This means in practice that, even in the energy region where the optical phonons exist, SiN behaves as a lossy dielectric material. However, one can show that it is still possible to have surface electromagnetic waves in this

material with properties that are similar to those of SPhPs. The surface waves in the interface between a dielectric like vacuum and a lossy dielectric like SiN are often referred to in the literature as Zenneck waves[41].

The similarities between SiN and SiO_2 are also evident in the spatial distribution of the surface Poynting vector, as illustrated in Fig. S14b. As in the SiO_2 case, the radiative heat transfer is very much concentrated at the tip apex as a consequence of the fact that NFRHT is dominated in this case by surface electromagnetic waves with very small penetration depths. Again, this is clearly at variance with the observations in the Au case (Fig. 4d).
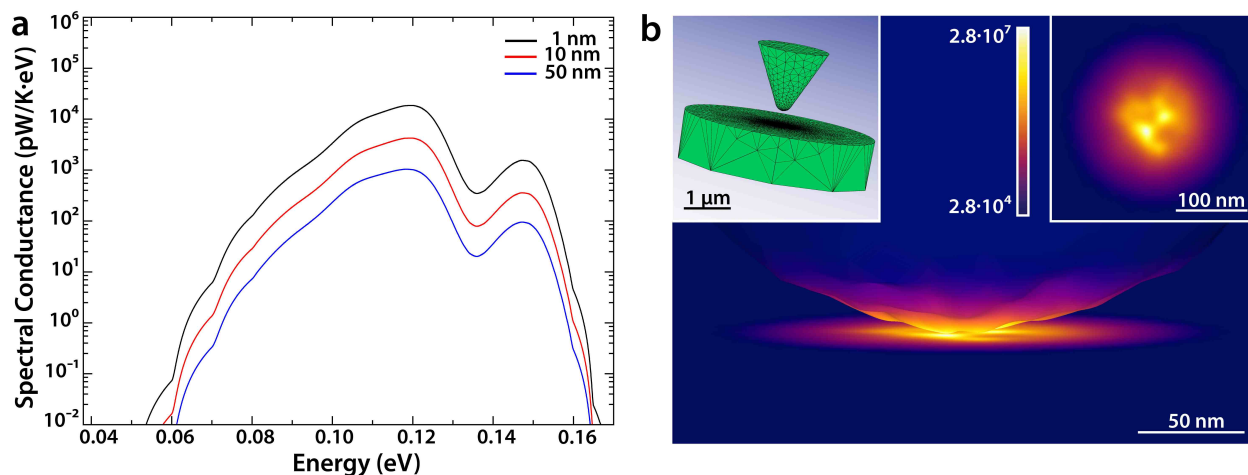

Figure S14. Spectral conductance and spatial distribution of the Poynting-flux for SiN. a, Spectral conductance as a function of the energy for a SiN tip-sample geometry for three different gap sizes. The tip radius is 175 nm and the reservoir temperatures are 310 K for the tip and 425 K for the substrate. Notice the logarithmic scale in the vertical axis. **b,** Surface-contour plot showing the spatial distribution of Poynting-flux pattern on the surface of the bodies for the SiN tip-substrate geometry of panel **a** with a gap of 1 nm. The colour scale has units of $W/(K \cdot eV \cdot m^2)$ and the plot has been computed at an energy of 0.12 eV, which corresponds to the maximum of the spectral conductance. The right inset shows the corresponding surface heat flux on the substrate, while the left inset displays the entire tip-sample geometry simulated along with the mesh used in the calculations.

16. Role of the Tip Roughness in the Calculations of eNFRHT

As explained both in the manuscript and in section 14, in our simulations we have taken into account the roughness present in our experimental probes. For completeness, we illustrate here the impact of the tip roughness. Towards this goal, in Fig. S15 we compare the results with and without roughness for the three materials investigated in this work (SiO_2, SiN and Au).
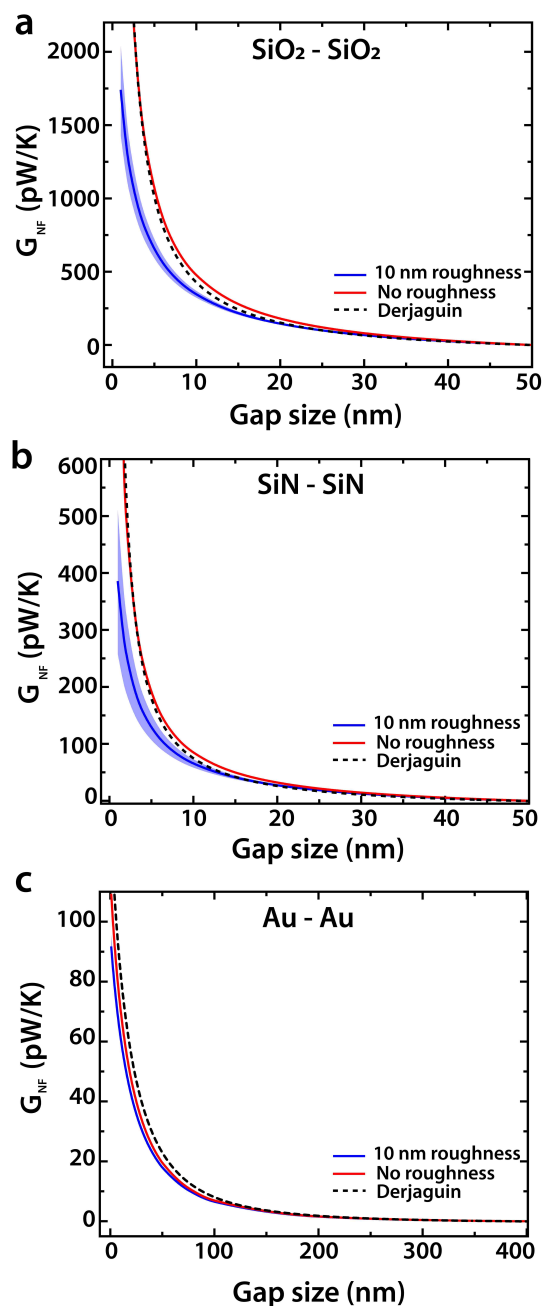
Figure S15. Role of the tip roughness. a, Computed near-field radiative conductance as a function of the gap size for a SiO_2 tip-sample geometry. The tip radius is 225 nm, and the reservoir temperatures are 310 K for the tip and 425 K for the substrate. The solid blue line corresponds to the average result obtained for 15 different tips featuring a roughness of 10 nm, while the blue shaded region represents the corresponding standard deviation. The red solid line corresponds to the result for an ideal tip without any roughness. The black dashed line corresponds to the result obtained using the proximity approximation, see text. **b,** The same as in panel **a,** but for a SiN tip-sample geometry. In this case the tip radius is 175 nm, and the reservoir temperatures are 310 K for the tip and 425 K for the substrate. **c,** The same as in panel **a**, but for a Au tip-sample geometry. In this case the tip radius is 450 nm, and the reservoir temperatures are 300 K for the tip and 301 K for the substrate.

From this comparison, one can draw two main conclusions: (i) the presence of roughness tends to reduce the radiative heat conductance and (ii) the roughness has a larger impact on the conductance of polar dielectrics. The first property is a simple consequence of the fact that the gap size is defined as the shortest tip-sample distance (following our AFM experiments). Thus, the presence of roughness effectively leads to an increase in the average tip-sample distance, as compared with the ideal tip with no roughness. This fact leads naturally to a reduction of the radiative heat transfer at a given gap size. Notice also that the impact of the roughness is obviously larger for the smallest gaps, where it can lead to a reduction of the conductance on the order of a factor of two, while it is negligible when the gap size becomes larger than the natural scale of the roughness (10 nm in our case). Furthermore, the larger impact of the roughness in the case of SiO_2 and SiN, as compared with Au, is again due to the fact that in polar dielectrics the radiative heat transfer is much more localized in the tip apex due to the excitation of SPhPs with very short penetration depths.

To conclude, it is interesting to compare the results for the ideal tips (with no roughness) with those obtained using the so-called proximity or Derjaguin approximation[42], which is frequently used to estimate the radiative heat transfer in complex geometries. For this purpose, we assume that the tips can be modelled by spheres of the same radius and compute the NFRHT between a sphere and an infinite plate. Within the proximity approximation, this calculation is done by assuming that the sphere is sliced into a series of infinitesimal annuli of different radii and the conductance between every annulus and the substrate is computed using the results for the NFRHT in a plate-plate geometry of the corresponding material. A more detailed description of this approximation can be found in section IIIA of the supplementary information of ref. 6. The results obtained with this approximation for the three materials considered in this work are shown in Fig. S15 (black dashed lines). It can be seen that this simple approximation provides a very good estimate of the gap-size dependent NFRHT in the case of the ideal tips. Therefore, it is clear that for ideal tips the proximity approximation can be used as a good first approximation to estimate the radiative heat transfer.

References:

33   Amick, H., Gendreau, M., Busch, T. & Gordon, C. Evolving criteria for research facilities: I – Vibration. 16 (2005).

34   Cappella, B. & Dietler, G. Force-distance curves by atomic force microscopy. *Surf. Sci. Rep.* **34**, 1-103 (1999).

35   Svetovoy, V. B., van Zwol, P. J., Palasantzas, G. & De Hosson, J. T. M. Optical properties of gold films and the Casimir force. *Phys. Rev. B* **77**, 035439 (2008).

36   Fujiwara, H. *Spectroscopic ellipsometry: principles and applications*. (John Wiley & Sons, 2007).

37   http://homerreid.com/scuff-em.

38   Rao, S. M., Wilton, D. R. & Glisson, A. W. Electromagnetic Scattering by Surfaces of Arbitrary Shape. *IEEE T. Antenn. Propag.* **30**, 409-418 (1982).

39   Palik, E. D. *Handbook of optical constants of solids*. (Academic Press, 1985).

40   Ordal, M. A. *et al.* Optical-Properties of the Metals Al, Co, Cu, Au, Fe, Pb, Ni, Pd, Pt, Ag, Ti, and W in the Infrared and Far Infrared. *Appl. Optics* **22**, 1099-1119 (1983).

41   Zenneck, J. Breeding of even electromagnetic waves along an even conducting surface and its relation to radiotelegraphy. *Ann. Phys-Berlin* **23**, 846-866 (1907).

42   Derjaguin, B. V. Direct Measurement of Molecular Attraction between Solids Separated by a Narrow Gap. *Q. Rev. Chem. Soc.* **10**, 295-329 (1956).